Interlibrary Loan Services – FSU Community
James Elliott – Resource Sharing Manager
The Florida State University
R.M. Strozier Library
116 Honors Way
Tallahasee, Florida 32306-2047
Email: lib-borrowing@fsu.edu
Website: https://www.lib.fsu.edu/service/interlibrary-loan
Phone: 850.644.4466

Non-FSU Institutions:
Lib-Lending@fsu.edu
850.644.4171

Applied Energy 97 (2012) 656–666

Contents lists available at SciVerse ScienceDirect

Applied Energy

journal homepage: www.elsevier.com/locate/apenergy

Numerical analysis of injector flow and spray characteristics from diesel injectors using fossil and biodiesel fuels

Michele Battistoni *, Carlo Nazareno Grimaldi

University of Perugia, Department of Industrial Engineering, Via Goffredo Duranti, 67, 06125 Perugia, Italy

ARTICLE INFO

Article history:
Received 20 July 2011
Received in revised form 27 November 2011
Accepted 29 November 2011
Available online 27 December 2011

Keywords:
Biodiesel spray
Cavitation
Nozzle flow
Eulerian multiphase flow
Primary breakup
Coupled simulations

ABSTRACT

The aim of the paper is the comparison of the injection process with two fuels, a standard diesel fuel and a pure biodiesel, methyl ester of soybean oil. Multiphase cavitating flows inside injector nozzles are calculated by means of unsteady CFD simulations on moving grids from needle opening to closure, using an Eulerian–Eulerian two-fluid approach which takes into account bubble dynamics. Afterward, spray evolutions are also evaluated in a Lagrangian framework using results of the first computing step, mapped onto the hole exit area, for the initialization of the primary breakup model.

Two nozzles with cylindrical and conical holes are studied and their behaviors are discussed in relation to fuel properties.

Nozzle flow simulations highlighted that the extent of cavitation regions is not much affected by the fuel type, whereas it is strongly dependent on the nozzle shape. Biodiesel provides a slightly higher mass flow in highly cavitating nozzles. On the contrary using hole shaped nozzles (to reduce cavitation) diesel provides similar or slightly higher mass flow. Comparing the two fuels, the effects of different viscosities and densities play main role which explains these behaviors.

Simulations of the spray evolution are also discussed highlighting the differences between the use of fossil and biodiesel fuels in terms of spray penetration, atomization and cone-angle. Usage of diesel fuel in the conical convergent nozzle gives higher liquid penetration.

1. Introduction

Biofuels for transportation and for small power generation plants are becoming increasingly popular and also worldwide national legislations are promoting their usage. These types of fuels are renewable energy sources which have properties similar to petroleum diesel fuel, so their advantages in terms of fuel economy and environmental impact are well acknowledged. Most of actual diesel engines can operate using up to 10% of biodiesel blended with standard diesel. Usage of pure oils, even if largely blended, requires instead much more attention due to operational and durability issues. Biodiesel can be produced by a variety of biomasses, mainly through trans-esterification. Being oxygenated fuels, biodiesels contribute to the reduction of particulate matter and unburnt hydrocarbons. Increased NO_x emissions however can be an issue. Also, as a bio-derived product, it contributes to the reduction of net carbon dioxide emission [1–7].

Aiming at increasing the usage of biodiesel as pure fuel or as an important blend with actual diesel, several R&D key areas have been identified, ranging from fuel system to combustion characteristics up to exhaust gas after-treatment. Injection process plays a significant role in this framework, since performances of DI diesel engine are strongly affected by the fuel spray quality. Atomization process and spray development largely depends on nozzle design. Also injection strategies and engine calibration are of primary importance in determining the final output.

Biodiesel has usually higher density and viscosity than petroleum diesel. Also it is a mixture of few organic molecules characterized by high molecular mass, thus evaporation and cavitation properties are quite different compared to diesel: distillation occurs practically at constant temperature and saturation pressure is extremely low, at ambient temperature.

Many investigations have been conducted on combustion and emissions using biodiesel in compression ignition engines, mainly by the experimental standpoint. On the contrary, detailed studies of injection and spray atomization characteristics are less frequent in literature for biofuels, despite their fundamental importance is recognized.

Payri et al. [8] found that the injection system is significantly affected by higher density and viscosity of biofuel, since both needle motion and flow characteristics are altered. Their tests showed that biodiesel spray is characterized by higher penetration and lower angle, especially for long injection. For short injections, or low temperature cases, they noticed a reduction on the injected

* Corresponding author.
E-mail address: michele.battistoni@unipg.it (M. Battistoni).

0306-2619/$ - see front matter © 2011 Elsevier Ltd. All rights reserved.
doi:10.1016/j.apenergy.2011.11.080

Nomenclature

a	stable droplet diameter (m)
A'''	interfacial area density (m^{-1})
C_D	drag coefficient
C_E	Egler coefficient
C_R	condensation reduction factor (phase change)
D	bubble diameter; orifice diameter (m)
D_{32}	bubble Sauter mean diameter (m)
f	probability distribution function (m^{-1})
$\vec{f}_i$	body forces per unit mass of phase i (vector quantity) (N/kg)
k	turbulent kinetic energy (m^2/s^2)
k	factor: $(D_{in} - D_{out})/10$ with D in μm
m	mass (kg)
$\vec{M}_{ij}$	momentum interfacial exchange term between phases i, j (vector quantity) (Pa/m)
n	number of phases involved in the multi-fluid model
N'''	bubble number density (m^{-3})
P, p	pressure (Pa)
r	droplet radius; inlet edge rounding (m)
R	bubble radius (m)
Re	Reynolds number
R_j	source/sink of bubble number due to bubble–bubble interaction (coalescence, breakup)
R_{ph}	source/sink of bubble number due to phase change
R-P	Rayleigh–Plasset equation
$S^{(k)}$	moment of population $f(R)$, order k
SMD	Sauter mean diameter
SME	Soybean oil methyl ester
t	time
$\vec{T}_i$	Reynolds turbulent stress of phase i (vector quantity) (Pa)
T	Taylor number = $Z \cdot \sqrt{We_g}$
$\vec{v}_i$	velocity of phase i (vector quantity) (m/s)
We	Weber number = $\rho r v_{rel}^2/\sigma$
Z	Ohnesorge number = $\sqrt{We_l}/Re$
y^+	wall normal distance, dimensionless
α_i	volume fraction of phase i
Γ_{ij}	mass interfacial exchange term between phases i, j (kg/s/m^3)
Δp	pressure difference (Pa)
ε	turbulent dissipation rate (m^2/s^3)
Λ	wavelength of the most unstable surface wave (Wave model)
ν	kinematic viscosity (m^2/s)
ρi	density of phase i (kg/m^3)
σ	liquid surface tension (N/m)
$\vec{\tau}_i$	viscous shear stress of phase i (vector quantity) (Pa)
τ	characteristic time constant (s)
Φ_j	source/sink of interfacial area due to bubble–bubble interaction (coalescence, breakup)
Φ_{ph}	source/sink of interfacial area due to phase change
Ω	growth rate of the most unstable surface wave (Wave model)

Subscripts

1	liquid phase
2	vapor phase (dispersed phase)
b	bubble
D	drag
g	gaseous
in	inlet
l	liquid
out	outlet
ph	phase change
s	saturation
T	turbulent dispersion
v	vapor

fuel mass, due to high delay in the needle lift start as a consequence of increased viscosity. Priesching et al. [1] found similar results: injected mass was reduced at low engine loads, while at a high engine loads with long injection durations and high metal temperatures biodiesel and diesel practically give the same mass flow. Allocca et al. [9] analyzed various biofuel sprays both in evaporative and non-evaporative conditions. At ambient temperature biodiesel has lower penetration and slightly lower cone angle. Park et al. [10] found that the mass injection rate of the SME, which has a higher density than diesel fuel, is higher than that of diesel fuel despite its low injection velocity. Tip penetration was slightly higher for diesel, at different back pressures. Biodiesel had also a higher SMD than diesel fuel. They carried out also CFD simulations with good results compared to experimental observations. At higher temperature they found that the average SMD increased, due to the evaporation of small size drops. Grimaldi and Postrioti [11] found that biofuel delays start of injection, can favor spray penetration and decreases breakup time. Postrioti et al. [12] noticed that at high injection pressures biodiesel causes a decrease of the rising slope of the mass flow. They also observed strong effects on the injection duration, for a given energizing duration, which were attributed to the higher viscosity of the biofuel which altered needle movement.

Numerical investigation on nozzle fluid-dynamics and spray characteristics of biofuel are less commonly found in literature. Som et al. [13] presented a numerical approach for coupling nozzle fuel simulations with spray development. Averaged outlet quantities, like velocity, contracted area and turbulent kinetic energy are computed in a first step. Subsequently a Lagrangian spray calculation is started which makes use of these quantities for the initialization of a novel primary breakup model. Results showed that biodiesel had reduced tendency to form cavitation zone inside the nozzle, while diesel provided wide areas of vapor up to the orifice exit section. Spray simulations in non-evaporative conditions showed that biodiesel gives a slightly higher tip penetration, higher SMD and slightly lower cone angle.

Som et al. [14] also analyzed, numerically and experimentally, hole shape and hydrogrinding effects on biodiesel sprays. They found that conicity significantly reduces cavitation and turbulence levels inside the nozzle orifice, slowing down primary breakup process and thus leading to larger spray droplets, increased penetration and smaller cone angle.

From this brief literature review, it can be observed that results are not univocal, especially for spray behavior, when comparing diesel and biodiesel. However, only few researchers took into account the nozzle-orifice geometry and its surface finish for interpreting spray behavior. Cavitation pattern can alter significantly atomization process and combined with different fuel properties this could lead to various types of results.

Also experimental investigations, when changing the fuel, are affected by changes in the needle movement which are hardly predictable.

In this framework, the main purpose of the work was the CFD analysis of the injector behavior with a standard diesel and a soybean biodiesel. Analyses are also extended to two different types of holes: a cylindrical sharp hole, highly cavitating, and a conical hole with edge rounding, with reduced cavitation characteristics.

Two-phase transient inner nozzle flow simulations were carried out for given injection pressure and backpressure levels. Cavitation fields, along with all other thermo-physical properties are computed up to the hole exit. Needle movement was prescribed identical for all fluids and hole shapes, thus avoiding additional effects on the results.

Detailed spray calculations have been subsequently carried using a sort of dynamic coupling to properly start droplets. A comprehensive model which accounts for aerodynamics, turbulence and cavitation induced effects for droplet primary breakup has been used. This model makes use of the spatial and temporal distribution of the flow quantities computed in the first step at the hole exit area to initialize the parcels of droplets, which, at each time step, are released from random locations within the exit cross section area. Thus, local starting characteristics are predicted in a realistic manner, enabling, as an example, the ability to predict also spray asymmetries.

Main objective of this paper is to analyse the processes involved in the atomization of biodiesel compared to diesel fuel at ambient temperature. Furthermore comparison with experimental data about tip penetration is also carried out.

The work was carried out using the commercial CFD software, AVL-Fire [15].

Prior to this work, authors carried out a validation study on the multi-fluid model and related results can be found in [16]; furthermore extensive references and validations about the nozzle and spray coupling using this approach can be found in [17–19].

2. Computational models: two stage coupling

Calculation procedure was split into two different parts, performing a "quasy-dynamic" coupling between the solution of the transient flow field inside the injector and the computation of spray development in the outside domain.

Simulations of the 3D unsteady multi-phase flow inside the injector were performed using an Eulerian–Eulerian approach. The results from the nozzle flow calculations, i.e. time-varying local distributions of flow field variables at the orifice exit, were stored and used later as input for the primary breakup model in spray simulations.

This approach introduces effects of nozzle flow turbulence and partial vapor formation into the atomization modelling.

Outside the injector, two-phase flow simulations for the atomization and spray development were performed using a typical Eulerian–Lagrangian approach.

In practice, two groups of simulations were combined in the sense that the boundary and initial conditions for the spray calculations at the injector outlet were obtained from the 3D inner nozzle flow results. A brief description of both computational approaches is provided below.

3. Injector flow simulations

An Eulerian multi-fluid method for the simulation of a two-phase flow in cavitating conditions is used [15,20]. The approach is non-homogeneous, i.e. momentum equations are solved separately for each phase. In the current application the multi-phase flow comprises liquid and its vapor and it is supposed isothermal. Each phase is viewed as a continuous medium, based on the assumption of interpenetrating continua, and for each one a set of conservation equations is solved. An ensemble averaging procedure is applied to remove the microscopic interfaces, at sub-grid scale level.

The model averaged equations of the multi-fluid approach are given in Table 1, according to Drew and Passman [21], where α, ρ, $\vec{v}$ and p are the averaged volume fraction, density, velocity and pressure, respectively, $\vec{\tau}$ and $\vec{\tau}$ are shear stress due to the molecular viscosity and turbulent Reynolds stress, the subscript i is the phase indicator, Γ is the phase change rate and $\vec{M}$ is the interfacial momentum transfer term including the drag and turbulent dispersion forces.

These equations are analogous to their single-phase counterpart, i.e. Reynolds-Averaged-Navier-Stokes equations, with the addition of a new scalar quantity, the volume fraction, and the relevant interfacial exchange terms for mass and momentum. These additional new terms have to be modelled, to close the system, on a physical basis.

In addition, a turbulence closure model is also needed, separately for each phase. Here, in Table 1, equations have been omitted for brevity. In this paper, the k–ζ–f model is adopted with a hybrid wall treatment for all y^+ values as turbulence closure model [15,22,23].

In a multi-phase flow, turbulent stresses in the continuous phase are computed by adding to the standard turbulent viscosity, $v_{t,SI}$ induced by shear and turbulence effect, a bubble induced viscosity term $v_{t,BI}$ as proposed by Sato and Sekoguchi [24].

Calculations have been performed assuming constant densities for both liquid and vapor. The main reasons for this are due to the well-known numerical issues if dealing with compressible media in multi-phase simulations with very high pressure gradients, like those found in diesel injectors.

3.1. Cavitation model

The interfacial exchange terms, relevant for two-phase cavitation, are the mass exchange Γ_{12} and the momentum exchange $\vec{M}_{12}$ terms, which take into account, at the grid scale level, the microscopic effects exerted at the interface between phases. Subscripts 1 or l refer to liquid, 2 or v refer to vapor. Additionally, the vapor phase is also called the dispersed phase.

3.1.1. Mass exchange term Γ_{12}

For cavitation phenomena, one of the key elements is predicting the vaporization rate, i.e. the rate of mass exchange Γ_{12} between liquid and vapor, determined by the rate of change of bubble vapor mass due to isothermal evaporation or condensation. In this paper a general, non-linear form of the Rayleigh–Plasset equation is used to describe bubble growth dynamics [15,25]. The following Table 2 shows the model equations.

Table 1
Conservation equations for phase i, with $i = 1,\ldots,n$.

$\frac{\partial \alpha_i \rho_i}{\partial t} + \nabla \cdot \alpha_i \rho_i \vec{v}_i = \sum_{\substack{j=1 \\ j\neq 1}}^{n} \Gamma_{ij}$	Mass
$\frac{\partial \alpha_i \rho_i \vec{v}_i}{\partial t} + (\nabla \cdot \alpha_i \rho_i \vec{v}_i)\vec{v}_i = -\alpha_i \nabla p + \nabla \cdot \alpha_i (\vec{\tau}_i + \vec{T}_i) + \alpha_i \rho_i \vec{f}_i + \sum_{\substack{j=1 \\ j\neq 1}}^{n} \vec{M}_{ij} + \vec{v}_i \sum_{\substack{j=1 \\ j\neq 1}}^{n} \Gamma_{ij}$	Momentum
$p = p_i$	Assumption
$\sum_{i=1}^{n} \alpha_i$	Compatibility eq.
Omitted for brevity, see [15,20,21]	Turbulent kinetic energy
Omitted for brevity, see [15,20,21]	Turbulent dissipation rate
$v_t = v_{t,SI} + v_{t,BI}$ where $v_{t,BI} = C_{Sato} D_b \lvert \vec{v}_1 - \vec{v}_2 \rvert \alpha_d$	Turbulent viscosity of continuous phase

Table 2
Mass exchange model equations.

$\frac{\partial m_b}{\partial t} = \rho_2 4\pi R^2 \dot{R}$	Bubble mass change rate
$\frac{\Delta p}{\rho_l} = R\ddot{R} + \frac{3}{2}\dot{R}^2$	Rayleigh–Plasset equation (non-linear form)
$\Delta p = p_s - (p - C_E \frac{2}{3}\rho_l k_l)$	Effective pressure difference
$\Gamma_{12} = \frac{N'''}{C_R} \cdot \frac{\partial m_b}{\partial t} = \frac{N'''}{C_R}\rho_2 4\pi R^2 \sqrt{\frac{2}{3}\left(\frac{\Delta p}{\rho_1} - R\ddot{R}\right)}$	Mass exchange during cavitation

Table 3
Momentum exchange model equations.

$\vec{M}_{12} = C_D \frac{1}{8}\rho_1 A'''\lvert\vec{v}_1 - \vec{v}_2\rvert \cdot (\vec{v}_2 - \vec{v}_1) + C_T \rho_1 k_1 \nabla\alpha_2$	Drag and turbulent dispersion forces
$C_D = \begin{cases} 192(1 + 0.10Re^{0.75})Re^{-1} & Re \le 1000 \\ 0.438 & Re > 1000 \end{cases} \quad Re = \frac{\lvert\vec{v}_1 - \vec{v}_2\rvert D_b}{v_1}$	Drag coefficient for spherical bubbles

Table 4
Poly-dispersed model.

$\frac{\partial N'''}{\partial t} + \nabla \cdot (N''' \vec{v}^{(0)}) = \sum R_j + R_{ph}$		Transport eq. for bubble number density
$\frac{\partial A'''}{\partial t} + \nabla \cdot (A''', \vec{v}^{(2)}) = \sum \Phi_j + \Phi_{ph}$		Transport eq. for interfacial area density
$S^{(k)} = \int_0^\infty R^k f(R) dR$	$\vec{v}^{(k)} = \frac{1}{S^{(k)}} \int_0^\infty \vec{v} R^k f(R) dR$	$S^{(0)} = N'''$
		$4\pi\, S^{(2)} = A'''$
		$(4/3)\pi\, S^{(3)} = \alpha_2$

For evaporation $C_R = 1$, whereas for condensation, due to lack of modelling to reflect the fact subcooled vapor could exist in fast transients, the same formulation is assumed with the introduction of a condensation reduction coefficient usually greater than one, $C_R \geqslant 1$, which retards the rate of bubble condensation and it could be used as a tuning constant of the model. $C_R = 5$ was used in this work.

An additional term is also included, proposed by Egler [15,26], which accounts for the turbulent pressure fluctuations. C_E was set to 1.2 in this work.

3.1.2. Momentum exchange term $\vec{M}_{12}$

Interfacial momentum exchange is modelled taking into account drag and turbulent dispersion effects; inertia and lift effects are neglected. Table 3 summarizes the model equations. Drag on a bubble is obtained assuming spherical shape, using a drag coefficient C_D depending on Reynolds number. The turbulent mixing process between phases is associated to the momentum interaction at the interface, which induces turbulence production on the liquid phase through Sato model, shown previously. Turbulent dispersion force relates bubble diffusion to the continuous phase turbulent kinetic energy and dispersed phase volume fraction gradient. $C_T = 0.1$ was used in this work.

3.2. Poly-dispersed bubble size model

The state of bubble diameter can be modelled as mono-dispersed (i.e. of uniform size all over the domain) or as poly-dispersed (function of position and time). The latter has been chosen in this work and, being more general, is useful or even mandatory in many applications where bubble size difference plays a significant role.

In general, a variable size dispersed phase system may be described by a probability distribution function for bubble size $f(R)$ [27,28]. Mathematically, by applying the moment method, it can be shown that it is sufficient to solve two transport equations for two additional scalars, the bubble number density N''' and the interfacial area density A''', as shown in Table 4. Through these two quantities, N''' and A''', the interfacial mass exchange Γ_{12} and momentum exchange $\vec{M}_{12}$ can be evaluated locally, since any other quantity can be obtained from these: as an example, Sauter mean diameter, which is used for determining the average drag force, is $D_{32,b} = 6\alpha_2/A'''$.

Further details on poly-dispersed flow implementation can be found in [15,27,28], where closure models for source terms, on the right hand side, are provided and discussed. The mechanisms taken into account are coalescence due to turbulent random collisions, breakup induced by turbulent impact and bubble generation due to phase change (vaporization of cavitation).

4. Spray simulations

The spray evolution modelling is practically approached adopting the so-called Discret Droplet Model (DDM) [29], where liquid droplets are grouped into parcels (each one characterized by equal diameter, velocity, etc.) which statistically describe the actual spray behavior. Tracking of each parcel trajectory is carried out in a Lagrangian framework, solving the momentum equation that takes into account the forces exchanged between continuum and dispersed phases.

Among all phenomena related to spray development, such as evaporation or droplet collision, breakup process is clearly recognized as the most important and still today has not been fully solved, see Fig. 1.

In practical implementation, droplet breakup rate is commonly approached through the velocity of loss of droplet radius r, as

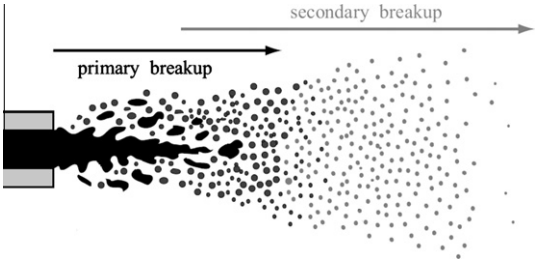

Fig. 1. Schematic of breakup processes.

expressed in the following equation, where a is a stable radius and τ is a characteristic breakup time.

$$\frac{dr}{dt} = \frac{r-a}{\tau}$$

Most of CFD codes aim at determining these two values, by adopting various sub-models.

Due to the very high injection pressures in diesel engines, it is not recommendable to uniformly handle the whole breakup process. Therefore, breakup phenomena occurring near the nozzle exit, where the initial liquid column is disintegrated into ligaments or droplets, are accounted for by primary breakup models, whereas prediction of further breakup process starting from initial drops is handled by secondary breakup models [17,18,30].

4.1. Primary breakup

The primary diesel breakup model is also based on the rate approach, and aims at capturing the combination of the aerodynamic mechanism, modelled through the Wave approach [31], and the turbulence mechanism with included cavitation effects [15,19]. Table 5 provides a brief summary of the primary breakup models, where C_i are model constants.

To account for these breakup forces, spatial and time resolved information concerning nozzle flow conditions is necessary. Basically this data are velocities, turbulence variables, densities, void fractions and cavitation bubble data. This is achieved using the results (written in a so called "nozzle file" format) of the first stage calculations about the Eulerian–Eulerian two-phase flow inside the nozzle. At each time step, the Lagrangian spray model reads the necessary data from the nozzle file, and applies the appropriate values for each droplet.

The Lagrangian spray parcels are randomly released inside the area of nozzle outlet cross-section. This method is supposed to offer great advantages since it delivers, at each time instant, appropriate local properties which depends on their physical release location.

In each time step breakup rate is calculated for all breakup mechanisms (aerodynamic and turbulent with enhancement due to cavitation bubble collapse) and the faster will be applied for the considered droplet. Obviously, the stable diameter and the characteristic time scale for each breakup mechanism are adjustable through parameters, thus some artificial influence is allowed (see C_i constants in Table 5).

Disintegration of the liquid core is modelled through the blob injection approach: introducing a series of large blobs of approximately nozzle diameter, the coherent liquid jet close to the nozzle is represent. Blob diameters are then quickly reduced according to the mass detachment rate calculated from the primary breakup model.

Droplets get also an initial radial velocity derived from aerodynamic respectively turbulent breakup mechanism. Thus the spray angle is calculated immediately from atomization physics. In this work, model constants have been set globally for all the simulated cases, without any specific tuning for the different fuels or nozzle shapes.

4.2. Secondary breakup

Secondary breakup accounts for the further diameter reduction of droplets which occurs outside the primary breakup length.

Table 5
Principal equations of primary breakup model.

$a = C_1 \Lambda$ $\tau = (3.726 C_2\ r)/(\Lambda\Omega)$	$\Lambda = f(r, Z, T, We_g)$ $\Omega = f(r, Z, T, We_g, \sigma, \rho_l))$	Wave model (Kelvin–Helmholtz instability)
$a = C_3 C_\mu^{0.75} \frac{k^{1.5}}{\varepsilon}$ $\tau = C_4 \frac{k}{\varepsilon}$	$\frac{dk}{dt} = -\varepsilon + S_k$ $\frac{d\varepsilon}{dt} = -C\frac{\varepsilon}{k}(\varepsilon - S_k)$	Turbulent breakup with cavitation effects (due to source term S_k)

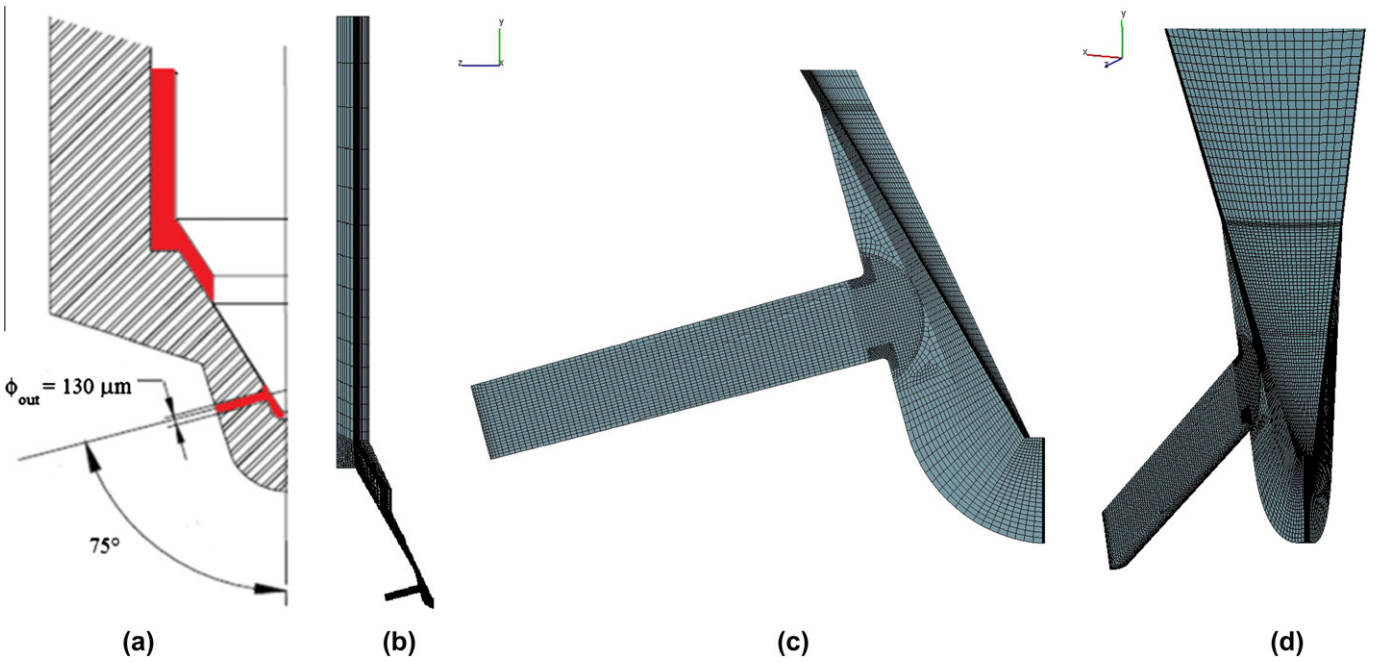

Fig. 2. Injector and mesh. (a) Section, (b) mesh global view, (c and d) mesh nozzle details.

Droplet shape was regarded as spherical and standard drag coefficients have been adopted as a function of Re number: momentum exchange is then allowed. Secondary breakup is accounted for using the Wave model [31] based on the Kelvin–Helmholtz instability of growing surface waves. Main tuning constants were set to $C_1 = 0.61$ and $C_2 = 20$. Primary and secondary breakup do not act at the same time on the parcels, but subsequently. The criterion for switching from primary to secondary breakup are a check on critical transition Weber number and checks on stable or minimum diameter.

Additional sub-models were clearly necessary to fully describe the Lagrangian phase dynamics. Gosman–Ioannidis model [32] has been used for droplet turbulent dispersion. Droplet collisions have been accounted for adopting the standard Schmidt–O'Rourke approach [15].

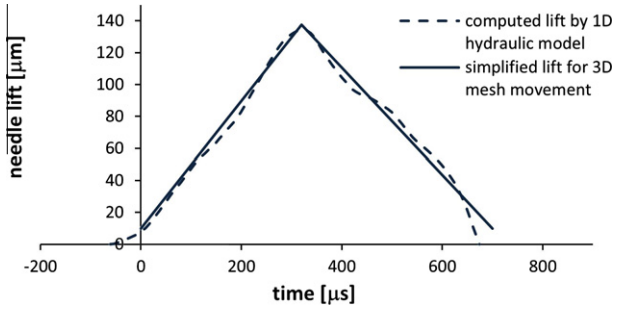

Fig. 3. Needle movement. Energizing time = 500 μs, injection pressure = 1350 bar, ambient pressure = 10 bar.

5. Injector CFD model

The internal geometry of a Bosch CRI1 common-rail injector was modelled, as it is shown in Fig. 2. Nozzle type is mini-sac and has 5 equally spaced holes, with outlet diameter of 130 μm and hole length of 700 μm [12,16]. Two hole shapes were studied: a cylindrical orifice shape (k-factor = 0) with a practically sharp edge (2 μm of edge rounding) and a conical shape (k-factor = 1.3) with a mid-level rounding at the inlet (10 μm of edge rounding).

Exploiting the symmetry of the injector, only one tenth of the fluid domain, i.e. 36° sector, was modelled. A moving grid was built, with a very fine mesh of about 200'000 total cells; the hole was meshed with 120,000 cells (with average size of 5 μm and refinements near the inlet edge up to 1.2 μm); the remaining sac and body comprised about 80,000 cells. A cylindrical, non-conformal interface

Table 6
Fuel properties at ambient temperature, Refs. [16,35–37].

Fuel	Liquid phase			Vapor phase		Saturation pressure (Pa)
	Density (kg/m^3)	Dynamic viscosity (Pa s)	Surface tension (N/m)	Density (kg/m^3)	Dynamic viscosity (Pa s)	
EU diesel	825	0.0021	0.024	5.0	10^{-5}	1000
SME biodiesel	870	0.0039	0.028	8.5	10^{-5}	1

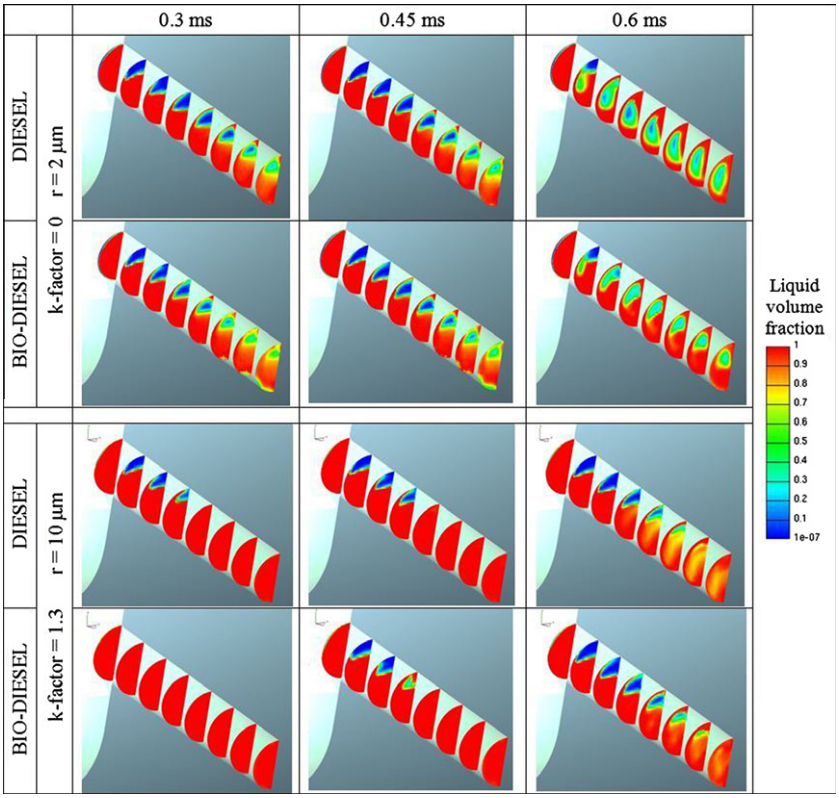

Fig. 4. Liquid volume fractions at 0.3 ms, 0.45 ms and at 0.6 ms after SOI.

exists between the hole mesh block and the remaining mesh block, which is positioned sufficiently inside the sac volume to minimize discretization errors near the inlet edge zone. Movement of the needle surface was obtained by stretching and shrinking suitable buffer cells (in the needle seat and sac zones). A value of 10 μm was used as minimum needle lift to avoid zero thickness cells. The needle lift law was computed by means of a 1D hydraulic model of the injector, as reported in [33,34], and it is shown in Fig. 3. Simulations refer to an injection pressure of 1350 bar, an outlet ambient pressure of 10 bar and an electrical energizing time of the electro-injector of 0.5 ms. The simulated total physical time was 0.7 ms and the time step ranged from 1.0E−8 s to 5.0E−7 s, with smaller values used during the starting phase [16].

The pressure values were specified at the inlet and outlet boundaries, while symmetry conditions were employed on the two sides of the 36° sector mesh.

Fuels adopted for the comparative analysis were a standard European diesel and a Soybean Methyl Ester (biodiesel). Their properties at 40 °C are listed in Table 6.

The two-fluid model, already described, has been used with the implicit non-linear form of R-P equation for mass exchange and the poly-dispersed approach for bubble distribution.

6. Spray CFD model

Half domain of a constant volume vessel was represented, using approximately 450,000 cells, applying a symmetry condition. The half domain also perfectly matched and exploited the exit section of the nozzle simulations (half hole modelled). The spray region is characterized by a mesh size of 0.20 mm and it becomes gradually coarser outside of the spray zone. Mesh sensitivity studies were carried out at the beginning of the work [38,39]. Injector operating conditions were as follows: injection pressure = 1350 - bar, vessel back-pressure = 10 bar, vessel air temperature = 300 K.

7. Results of nozzle flow simulations

Some results of the 3D transient flow inside the injector are shown in this Section. The images in Fig. 4 show the liquid volume fraction in seven cuts through the axis of the nozzle hole. The maximum of gaseous fuel is in the blue regions and these are the areas of cavitation bubbles. The red regions contain pure liquid fuel.

In these types of injectors usually a cavitation zone develops around the region where the fuel enters the nozzle bore. From there a plume of fuel vapor spreads down to the exit of the nozzle when cylindrical nozzle with sharp edge is used (highly cavitating). On the contrary, usage of k-shaped nozzle reduces significantly the production of initial vapor, due to higher local pressures, and liquid flow reattaches before hole exit, thus fully exploiting the outlet section.

As far as fuel types are concerned, diesel gives only slightly wider regions of vapor formation, which indicates that generally diesel and biodiesel behave in a similar way form the cavitation standpoint. Differences in cavitation areas are quite small due to the very high range of pressure variation inside of the injector, compared to the saturation values. Despite saturation pressure values vary by three orders of magnitude for the two fuels (1000 Pa for diesel and 1 Pa for biodiesel), pressure levels fall from 1.35×10^8 Pa down to practically 0 Pa (absolute) just after the inlet edge, hence the range of variation is enormous compared to P_s values, thus triggering of cavitation is guaranteed and is almost independent of fuel the type. Some differences between fuels can anyway be appreciated looking at the time of cavitation incipit:

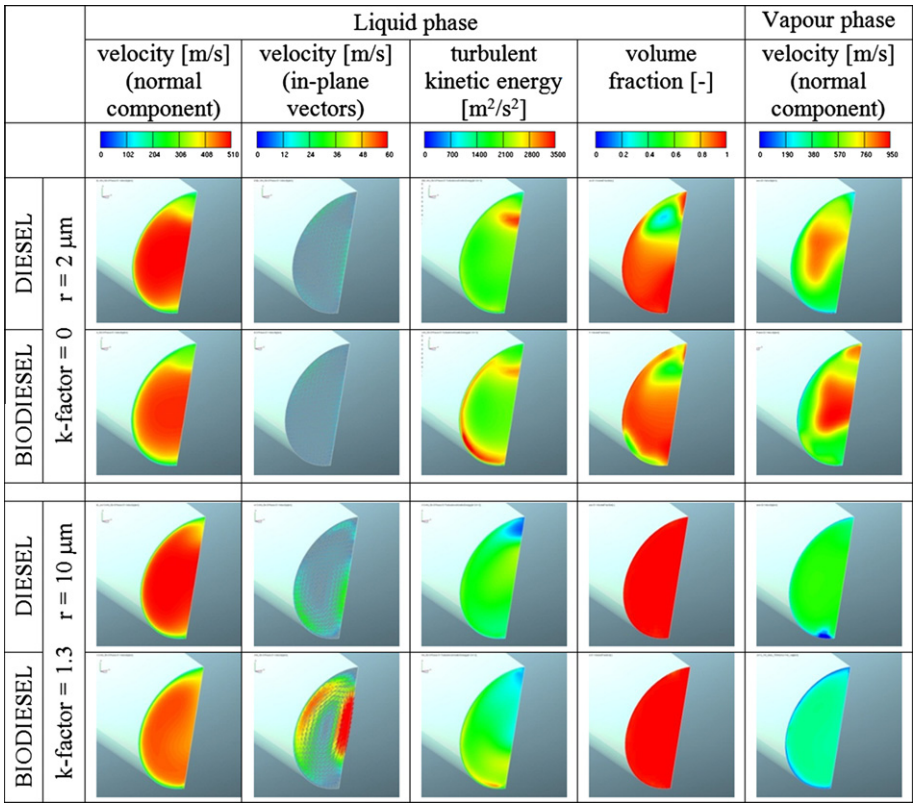

Fig. 5. Outlet flow field at 0.3 ms.

biodiesel shows some retard (see for example Fig. 4, *k*-factor = 1.3, timing 0.3 and 0.45 ms after SOI).

Outlet quantities, relevant for spray primary breakup model, are show exemplary at $t = 0.3$ ms in Fig. 5. Velocities, turbulent kinetic energy and volume fractions for the liquid phase and velocities for the vapor phase are shown. The selected time coincides with the already shown data of Fig. 4, first column.

Velocity components lying on the outlet plane are significant and also some vortices can be appreciated: these will contribute to the disintegration of the liquid column into droplets, determining also the spray near angle. Additionally turbulence field is very important for primary breakup. Its level is globally higher for the cylindrical (cavitating) shape. Distribution is very uneven and local peaks can be observed in the zones of shear layer between liquid and vapor formation and in the re-condensation region near the lower side of the walls. Biodiesel seems also to amplify the latter phenomenon.

In order to have a global overview of the injection evolution, the transient – mass averaged over exit section – outlet quantities are shown in the charts of Fig. 6, for the two fuels and the two hole shapes. Charts refer to the mass flow rate, the area occupied by the liquid fuel, the mass-averaged liquid velocity and the mass-averaged liquid turbulent kinetic energy.

Higher flow rates are achieved using the conical nozzle, as expected.

By the way, diesel and biodiesel achieve similar values with the cylindrical (cavitating) hole, whereas diesel slightly prevails when the hole is conical. Authors believe that the concurrent phenomena to take into account are:

- higher density causes higher mass flow, thus biodiesel can be benefited;
- lower viscosity causes an increase of the discharge coefficient and thus of the exit velocity; diesel can be benefited and this can be appreciated in Fig. 6c;
- cavitation reduces the effective area; biodiesel is slightly less cavitating as can be appreciated in Fig. 6b;

Keeping these effects in mind, mass flow curves, in Fig. 6a, can be interpreted. In the conical hole, both fuels exploit the full cross section (except in the last part of the injection), diesel has a significant higher outlet velocity and despite its lower density, it provides a higher mass flow. In cavitating conditions, where outlet effective sections are reduced, mass flow are pretty similar because, in addition to the above considerations, biodiesel produces a slightly lower cavitating area.

Average velocity values show that, independently of the effective outlet area (full or reduced due to cavitation), diesel has higher outlet velocity and this can be partly due to its lower density since velocity is proportional to $\sqrt{2\Delta p/\rho}$. However the square root of

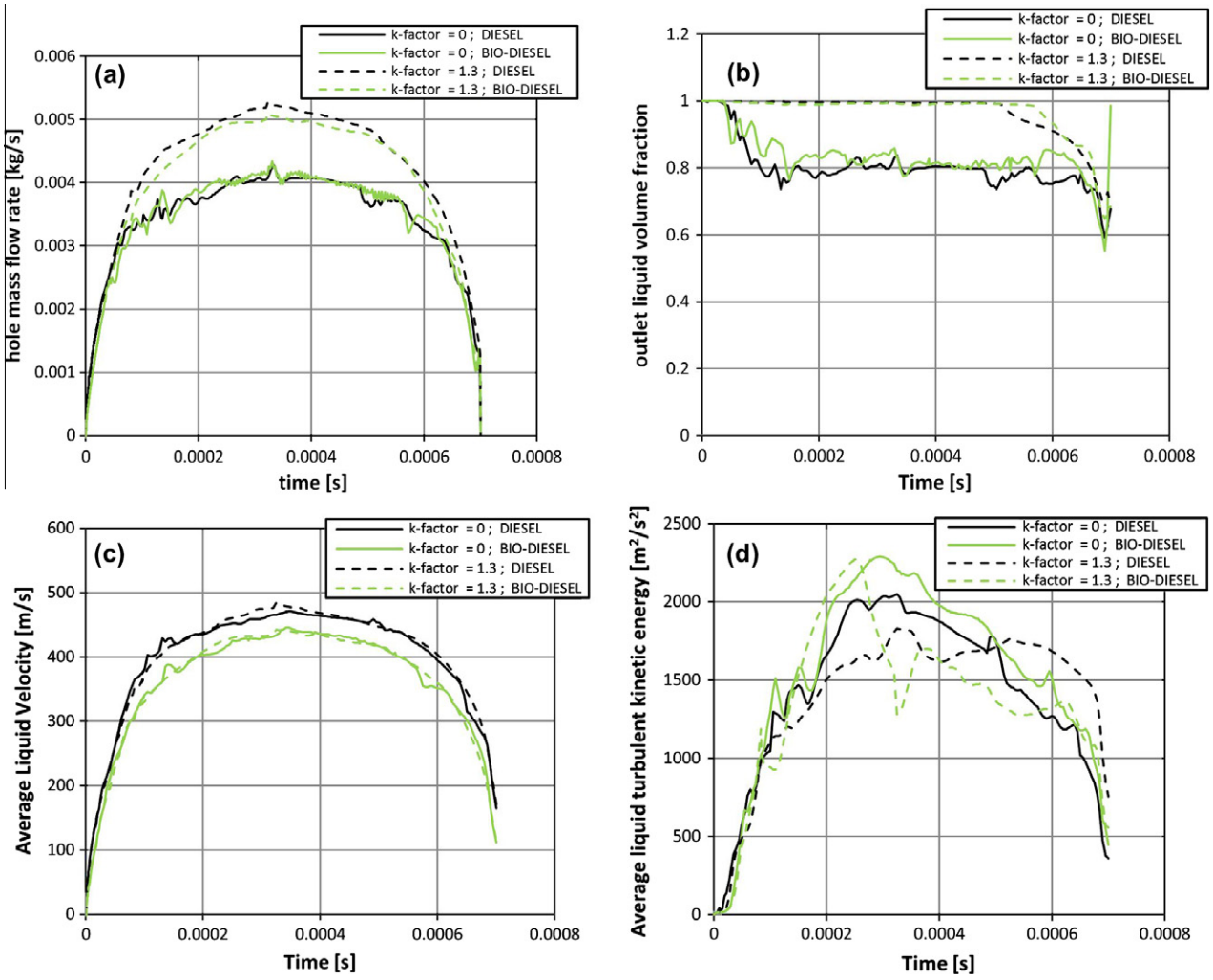

Fig. 6. Outlet integral quantities. (a) Mass flow rate, (b) area occupied by liquid fuel, (c) mass-averaged liquid velocity, (d) mass-averaged liquid turbulent kinetic energy.

densities ratio is not sufficient to justify all the difference between the two fuels, thus also lower pressure losses of diesel, due to its lower viscosity, have to be taken into account.

Finally, liquid turbulent kinetic energy seems to be generally higher for biodiesel, apart from the closing stage of the injection with the conical hole.

8. Results of spray simulations

Major results about spray calculation are shown in this Section. Spray structure and its development are shown in Fig. 7 at different times (0.1, 0.2, 0.3, 0.5, 0.7 ms from SOI).

Diesel and biodiesel produce similar cone angles using the cylindrical hole (k-factor = 0). Conversely, diesel angle is significantly smaller using the rounded and conical hole (k-factor = 1.3), while biodiesel produces a large cloud after the secondary breakup that increases significantly its global spray cone angle.

Biodiesel behaves similarly with both hole shapes. Diesel fuel, instead, appears more sensitive to the hole shape and it shows very different breakup characteristics: with conical hole diesel produces a faster and denser spray which remains compact for long time, whereas cavitating hole enhances diesel spray breakup.

Fig. 7 shows also some asymmetry on the spray distribution. Due to an asymmetric distribution of cavitation within the nozzle hole, as shown in the previous Fig. 4, the spray is slightly deflect towards the upper side, with respect to the geometrical hole axis. Due to better atomization, smaller droplets and an increased spray angle are produced on the cavitation upper side. The ability to predict such phenomena is due to the detailed modelling of the effects of bubble collapse outside the nozzle, in the dense core region where the primary breakup acts.

Fig. 8 presents the spray global parameters: tip penetration and Sauter mean diameter. Penetration can also be compared to available experimental data, shown in Fig. 9. Diesel spray emerging from the conical hole presents the higher liquid penetration. Diesel spray from the cylindrical hole and both biodiesel sprays, instead, have lower and similar penetration trends versus time. The trend is clearly visible also in the experimental results, thus calculations captured well this behavior.

As already observed, diesel fuel is more sensitive to the hole shape, thus the conical nozzle, which produces significantly higher exit velocities without cavitating areas, gives the higher spray penetration. Using biodiesel, hole shape does not affect spray penetration significantly, even if the conical shape provides again a slightly higher penetration.

Observing the results for SMD, biodiesel produces quite larger droplet diameters and its breakup process is slower. Main reasons are the lower velocities and the lower Weber numbers. With respect to SMD, hole shape has negligible effect. Only fuel properties determine the average stable non-evaporating droplet size.

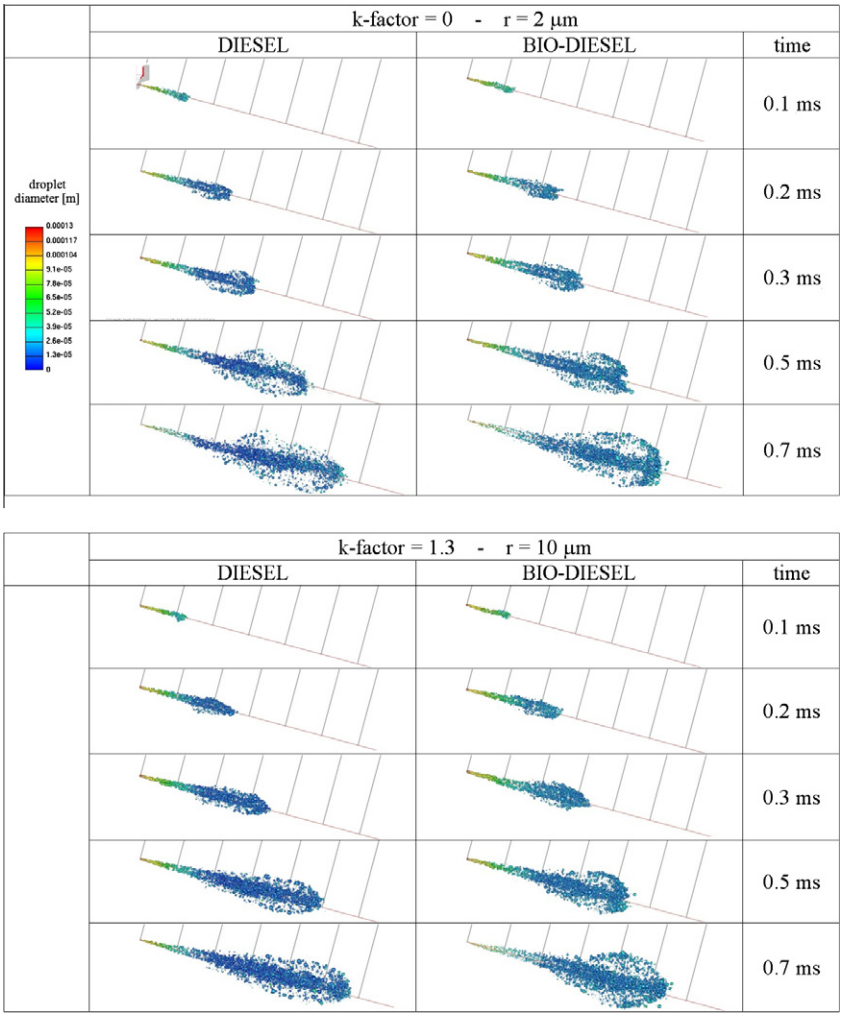

Fig. 7. Computed spray structures at different times. Color scale represents drop diameter, size represents parcel mass. (For interpretation of the references to color in this figure legend, the reader is referred to the web version of this article.)

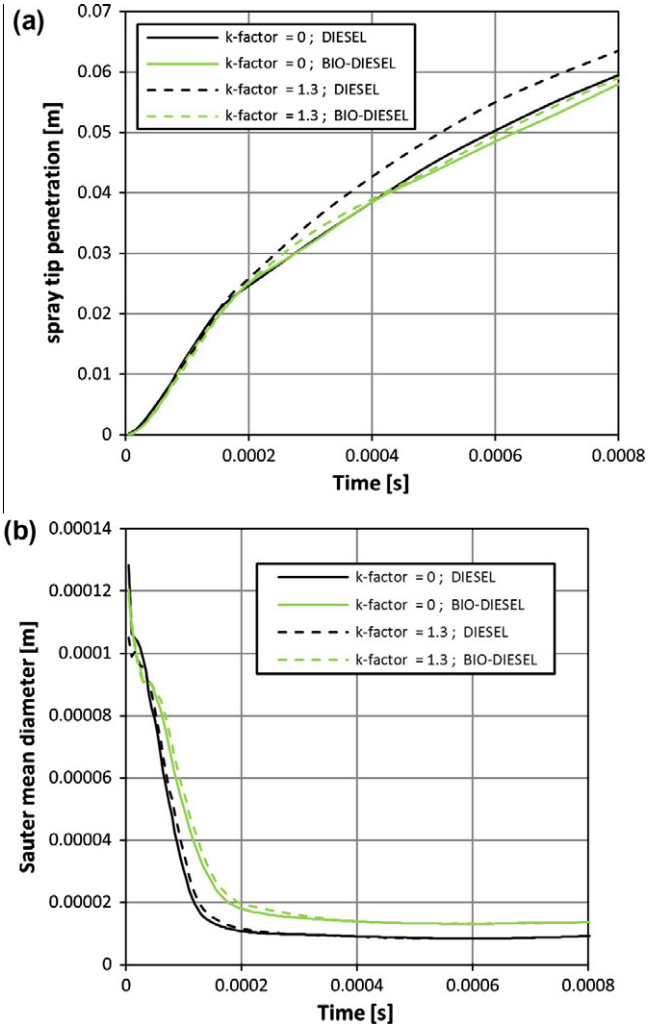

Fig. 8. Predicted spray evolutions. (a) Tip penetration and (b) Sauter mean diameter (over the entire domain).

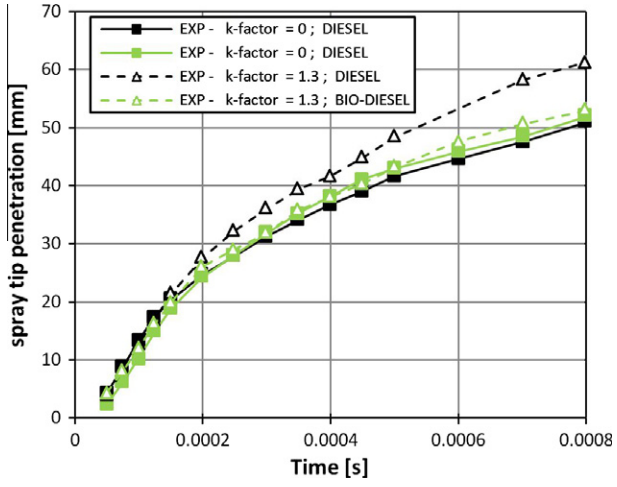

Fig. 9. Experimental data of spray tip penetration (from [12]).

9. Conclusion

The paper described a CFD study about nozzle flow and spray characteristics in a standard diesel injector, comparing two fuels, diesel and biodiesel, and two nozzle designs, with cylindrical and conical hole. Inner nozzle flow was coupled to spray evolution, using a two-step simulation methodology. As a result spray behavior predictions are based on a detailed (spatial and temporal) description of the flow properties at the hole exit area.

Primarily, fuel property effects were investigated, in terms of density, viscosity and vapor pressure. Among them, vapor pressure revealed to be of minor importance as far as inner nozzle flow field and mass flow rate are concerned.

Higher flow rates are achieved using the conical nozzle, since cavitation is strongly reduced.

Diesel provides slightly higher flow rate values than biodiesel when the hole is conical. Using cylindrical hole, which induces strong cavitation, mass flow rates are similar. These behaviors have been explained as effects mainly due to viscosity and density differences.

Diesel spray penetration and cone-angle are significantly affected by hole shape. Biodiesel spray, instead, is less sensitive to hole shaping. SMD is larger for biodiesel, irrespectively of hole shape. Diesel fuel in convergent conical nozzle provides significantly higher penetration and lower cone-angle. Good agreement is found with experimental measurements of spray tip penetration, suggesting that the simulation methodology is robust enough since it is able to take into account several phenomena occurring in the spray formation process and at the same time is able to predict consistent results.

References

[1] Priesching P, Pavlovic Z, Ertl P, Del Giacomo N, Beatrice C, Mancaruso E, et al. Numerical and experimental investigation of the influence of bio-diesel blends on the mixture formation, combustion and emission behavior of a modern HSDI diesel engine. SAE paper 2009-24-0041; 2009.
[2] Grimaldi CN, Postrioti LL, Battistoni M, Millo F. Common-rail Hsdi diesel engine combustion and emissions with fossil/bio-derived fuel blends. SAE paper 2002-01-0865; 2002.
[3] Postrioti L, Battistoni M, Grimaldi CN, Millo F. Injection strategies tuning for the use of bio-derived fuels in a common rail HSDI diesel engine. SAE paper 2003-01-0768; 2003.
[4] Patterson J, Hassan MG, Clarke A, Shama G, Helgardt K, Chen R. Experimental study of DI diesel engine performance using three different biodiesel fuels. SAE paper 2006-01-0234; 2006.
[5] Lujan JM, Tormos B, Salvador FJ, Gardar K. Comparative analysis of a DI diesel engine fuelled with biodiesel blends during the European MVEG-A cycle: preliminary study (I). Biomass Energy 2009;33(6-7):941–7.
[6] Lujan JM, Bermúdez V, Tormos B, Pla B. Comparative analysis of a DI diesel engine fuelled with biodiesel blends during the European MVEG-A cycle: performances and emissions (II). Biomass Energy 2009;33(6–7):948–56.
[7] Battistoni M. Experimental analysis of a common-rail DI diesel engine fuelled with bio-derived alternative fuels. PhD thesis, University of Perugia; 2004.
[8] Payri R, Desantes JM, Salvador FJ, Manin J. Influence on diesel injection characteristics and behavior using biodiesel fuels. SAE paper 2009-01-0851; 2009.
[9] Allocca L, Mancaruso E, Montanaro A, Vaglieco BM, Vassallo A. Renewable biodiesel/reference diesel fuel mixtures distribution in non-evaporating and evaporating conditions for diesel engines. SAE paper 2009-24-0054; 2009.
[10] Park SH, Kim HJ, Suh HK, Lee CS. A study on the fuel injection and atomization characteristics of soybean oil methyl ester (SME). Int J Heat Fluid Flow 2009;30:108–16.
[11] Grimaldi CN, Postrioti L. Experimental comparison between conventional and bio-derived fuels sprays from a common rail injection system. SAE paper 2000-01-1252; 2000.
[12] Postrioti L, Grimaldi CN, Ceccobello M, Di Gioia R. Diesel common rail injection system behavior with different fuels. SAE paper 2004-01-0029; 2004.
[13] Som S, Longman DE, Ramirez AI, Aggarwal SK. A comparison of injector flow and spray characteristics of biodiesel with petrodiesel. Fuel 2010;89:4014–24.
[14] Som S, Ramirez AI, Longman DE, Aggarwal SK. Effect of nozzle orifice geometry on spray, combustion, and emission characteristics under diesel engine conditions. Fuel 2011;90:1267–76.
[15] Avl List GmbH. AVL Fire v.2009: CFD solver, Eulerian multiphase. ICE Physics & Chemistry; 2009.
[16] Battistoni M, Grimaldi CN. Analysis of transient cavitating flows in diesel injectors using diesel and biodiesel fuels – SAE paper 2010-01-2245. Int J Fuels Lubricants 2010;3(2):879–900.
[17] von Berg E, Edelbauer W, Tatschl R, Alajbegovic A, Volmajer M, Kegl B, et al. Validation of a CFD model for coupled simulation of nozzle flow, primary fuel jet break-up and spray formation. In: Proceedings of the 2003 spring technical

conference of the ASME internal combustion engine division, May 11–14, 2003 Salzburg, Austria; 2003.
[18] Kadocsa A, Tatschl R, Kristóf G. Modelling of diesel injection process using a primary breakup approach. In: Proceedings of the conference on modelling fluid flow (CMFF'06), Budapest, Hungary, September 6–9, 2006.
[19] Tatschl R, Künsberg Sarre C, Alajbegovic A, Winklhofer E. Diesel spray modelling including multidimensional cavitation nozzle flow effects. In: Proceedings of ILASS-Europe conference, September 11–13, Darmstadt, Germany; 2000.
[20] Alajbegovic A, Grogger HA, Philipp H. Calculation of transient cavitation in nozzle using the two-fluid model. In: Proceedings of the Conference ILASS-Americas 99, 1999.
[21] Drew DA, Passman SL. Theory of multicomponent fluids. New York: Springer; 1998.
[22] Hanjalic K, Popovac M, Hadziabdic M. A robust near-wall elliptic relaxation eddy-viscosity turbulence model for CFD. Int J Heat Fluid Flow 2004;25(6): 1360–78.
[23] Popovac M, Hanjalic K. Compound wall treatment for RANS computation of complex turbulent flows and heat transfer. Int J Heat Fluid Flow 2007;78(2): 177–202.
[24] Sato Y, Sekoguchi K. Liquid velocity distribution in two-phase bubble flow. Int J Multiphase Flow 1975;2(79).
[25] Brennen CE. Fundamentals of multiphase flows. Cambridge University Press; 2005.
[26] Hinze JO. Turbulence. New York: McGraw-Hill; 1975.
[27] Ishii M. Thermo fluid dynamic theory of two-phase flow. Paris: Eyrolles; 1975.
[28] Ishii M, Sun X, Kim S. Modeling strategy of the source and sink terms in the two-group interfacial area transport equation. Ann Nucl Energy 2003;30(13):1309–31.
[29] Dukowicz JK. A particle-fluid numerical modes for liquid sprays. J Comput Phys 1980;35:229–53.
[30] Tatschl R, Künsberg Sarre, CV, Berg E. IC-engine spray modeling – status and outlook. International multidimensional engine modeling user's group meeting at the SAE congress 2002.
[31] Reitz RD. Modeling atomization processes in high-pressure vaporizing sprays. Atom Spray Technol 1987;3:309–37.
[32] Gosman AD, Ioannides SI. Aspects of computer simulation of liquid-fuelled combustors. AIAA, J Energy 1983;7(6):482–90.
[33] Postrioti L, Grimaldi CN, Ubertini S, Bella G. Study of the influence of the injection system in a multi-dimensional spray simulation. SAE paper 2005-24-088; 2005.
[34] Foschini L. Analisi numerica 1D di un sistema di iniezione Common Rail Bosch. MS Thesis, University of Perugia; 2004.
[35] Yuan W, Hansen AC, Zhang Q. Vapor pressure and normal boiling point predictions for pure methyl esters and biodiesel fuels. Fuel 2005;84(7–8):943–50.
[36] Yuan W, Hansen AC, Zhang Q. Predicting the temperature dependent viscosity of biodiesel fuels. Fuel 2009;88(6):1120–6.
[37] Allen CAW, Watts KC, Ackmanb RG. Predicting the surface tension of biodiesel fuels from their fatty acid composition. J Am Oil Chem Soc 1999;76(3):317–23 [Paper no. J8912].
[38] Postrioti L, Mariani F, Battistoni M, Mariani A. Experimental and numerical evaluation of diesel spray momentum flux – SAE paper 2009-01-2772. SAE Int J Engines 2010;2(2):287–99.
[39] Postrioti L, Battistoni M. Evaluation of diesel spray momentum flux in transient flow conditions. SAE paper 2010-01-2244, proceedings of SAE Powertrains, fuels and lubricants meeting, October 2010, San Diego, USA; 2010.